A. NEIMITZ*,#, U. JANUS*

VOIDS NUCLEATION AT INCLUSIONS OF VARIOUS SHAPES IN FRONT OF THE CRACK IN PLANE STRAIN

An analysis is presented of the stress field in and around inclusions of various shapes. Results were obtained by the finite element method. Inclusions were located within elementary cells located at the centre of the specimen next to the crack front. The influence of an in-plane constraint on the stress distribution was tested.

*Keyword*s: void nucleation, inclusion fracture, critical stress

1. Introduction

In the accompanying paper [1] the possibility of void nucleation at the inclusions in uniaxial tensile stress state was discussed, based on the micro-structural observation of the failure evolution in the high-strength Hardox-400 steel. Inclusions in this steel assume various shapes, chemical compositions, and different level of homogeneity as well as orientations with respect to the loading direction. Inclusions of complex structures, consisting of several components may fracture at relatively low level of straining, less than 1%; while uniform inclusions such as nitride titanium or manganese sulfides require strain 1.5% and higher. Nucleation of voids took place at large inclusions from 1 to 3 micrometers in size. Fracture of the matrix was not observed even at large specimen elongation, much beyond the necking. The loading process was terminated before final failure. The chemical composition and the tensile properties of the Hardox-400 steel are presented in [1] and [2].

In this paper, the void nucleation process at inclusions is discussed, taking into account the constraints arising from the specimen geometry. The specimen contains a crack and the unit cell, containing void, is placed in front of the crack.

This paper follows another paper by authors [1] where the literature review on the subject was presented.

2. Numerical model

The unit cell in front of the crack is different than that used to simulate the void nucleation at the inclusion in the uniaxial tensile test. Because it is taken from the central part of the specimen in front of the crack, it is in a condition of plane strain. Thus, the inclusion is modelled as a long cylinder, because it does not deform together with a cell in the direction of specimen thickness (i.e., a large out-of-plane constraint). The cell is loaded in the direction perpendicular to the crack faces (u_z) and in the direction

perpendicular to the crack front (u_y). The smaller the ratio u_y/u_z (u_y being negative), the smaller the in-plane constraint level. The main purpose of this paper is to demonstrate the influence of the in-plane constraint on the stress level in and around the elastic inclusion. Multiple opening strain levels, constraint levels and inclusion shapes are investigated (see Fig. 1). Additionally, the influence of inclusion size (2 µm vs. 0.4 µm) on the stress level inside the inclusion is investigated.
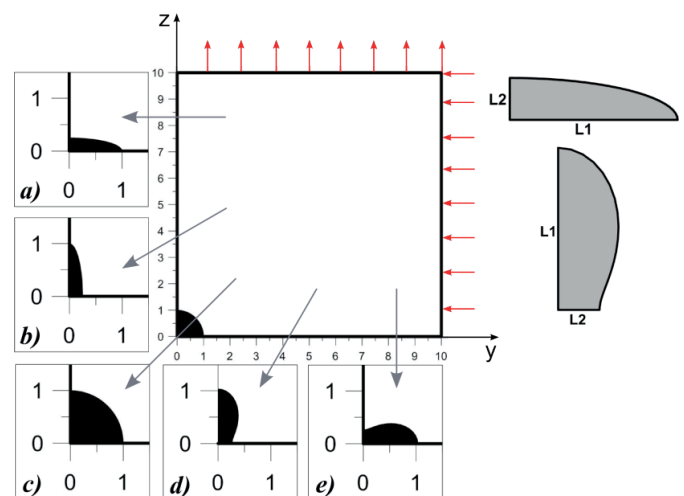

Fig. 1. Unit cell with various inclusion shapes

The loading of the elementary cell follows from the numerical analysis of the mechanical fields in front of the crack. The elementary cell was positioned at a distance of one average grain from the crack tip in the specimen centre. This location was selected to record the in-plane constraint imposed on the elementary cell in front of the crack. A paper by Galkiewicz [3] that discusses the T-stress influence on the elementary cell in front of the crack was used as a guide for simulation. Eq. (1) was formulated for the type of steel of interest, Hardox-400.

* KIELCE UNIVERSITY OF TECHNOLOGY, FACULTY OF MECHATRONICS AND MACHINE DESIGN, 7 TYSIĄCLECIA P.P. AV., 25-314 KIELCE, POLAND

Corresponding author: neimitz@tu.kielce.pl

$$\frac{u_y}{u_z} = 0.428 * \left(\frac{T}{\sigma_0}\right) - 0.338 \qquad (1)$$

This formula provides a relation between the T-stress and the ratio $\frac{u_y}{u_z}$. The value of u_z at the critical moment was estimated in [1]. The analysis was carried out assuming the inclusion to be a linear elastic material with Young's modulus E=300 GPa and Poisson's ratio ν=0.3. The uniaxial stress-strain curve was recorded in the experiment and implemented into Adina code. The finite element mesh for one selected example of inclusion geometry is shown in Fig. 2. Only a quarter of the unit cell was analysed because of the symmetry. The maximum inclusion size for each proposed shape was 2 μm. The aspect ratio (the ratio of the maximum to minimum size) of the ellipsoidal (Figs 1a, 1b) and elongated (Figs 1d, 1e) inclusions was $\frac{L_1}{L_2} = 4$.
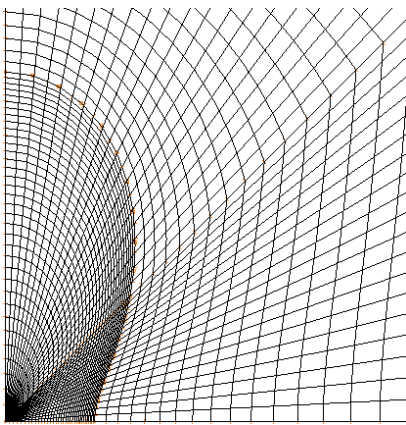

Fig. 2. Finite element mesh

Numerical computations were carried out for four levels of strain (1%, 1.2%, 1.5% and 3%) and three levels of the in-plane constraint (u_y/u_z=-0.3, -0.5 and -0.7). Fig. 3 shows an effective accumulated plastic strain distribution, computed at the central part of the specimen at 20°C. The specimen was SEN(B). The relative length of the crack was $\frac{a}{W} = 0.5$, where a is a crack length and W is the specimen width, and

the specimen thickness was 20 mm, satisfying in excess the plane strain requirements. The specimen was made of the Hardox-400 steel. A crack started growing at a deflection of 1.237 mm. The dashed line was registered at the critical moment, the dash-dot line was registered at 66% of the critical loading, and the solid line was registered at 33% of the critical loading. The vertical lines indicate the location of the unit cell and the location of maximum opening stress.
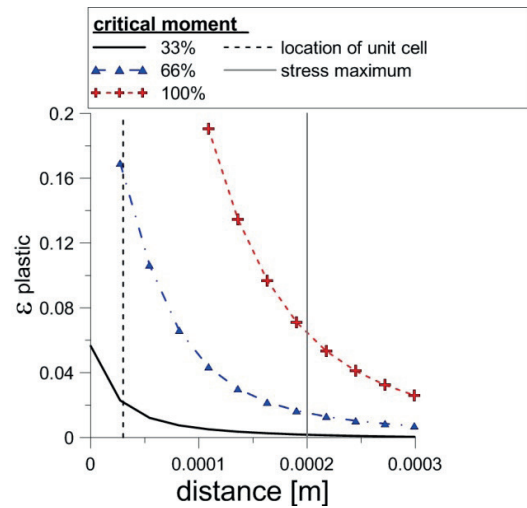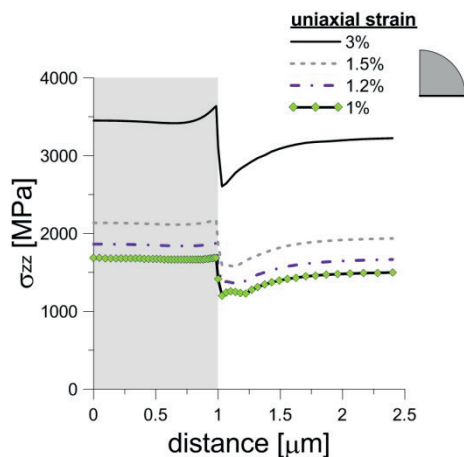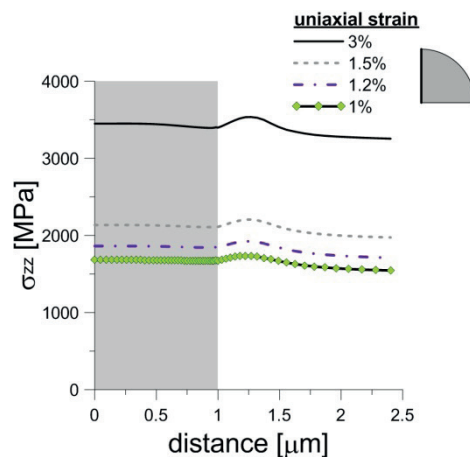

Fig. 3. The strain distributions in front of the crack for different stages of specimen loading

It can be observed from the strain distribution shown in Fig. 3 that the process of void nucleation close to the crack tip started early in the loading process.

3. Numerical results

Selected results are presented here from all the combinations of inclusion geometries and orientations that were tested. These results correspond to the geometries shown in Figs 1a, 1c, and 1d. In Fig. 4, the stress distributions calculated for u_y/u_z=-0.5 are presented. Selected numerical results are shown in Tables 1-3.

Fig. 4a. (Cylindrical inclusion.) Opening stress (σ_{zz}) distribution along the horizontal line. u_y/u_z=-0.5

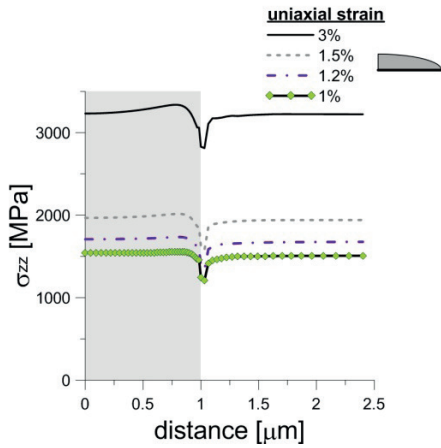Fig. 4b. (Cylindrical inclusion.) Opening stress (σ_{zz}) distribution along the vertical line. u_y/u_z=-0.5

Fig. 4c. (Inclusion of elliptical cross-section with the major axis oriented perpendicular to the loading direction.) Opening stress (σ_{zz}) distribution along the horizontal line. u_y/u_z=-0.5
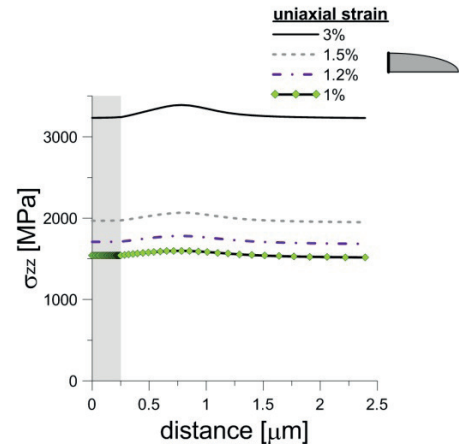

Fig. 4d. (Inclusion of elliptical cross-section with the major axis oriented perpendicular to the loading direction.) Opening stress (σ_{zz}) distribution along the vertical line. u_y/u_z=-0.5

Fig. 4e. (Inclusion of elongated cross-section (Fig. 1d) with the longest axis oriented parallel to the loading direction.) Opening stress (σ_{zz}) distribution along the horizontal line. u_y/u_z=-0.5
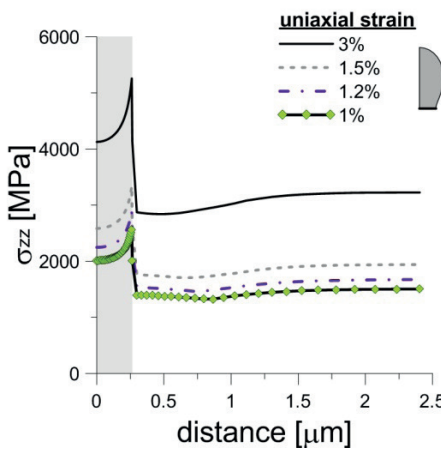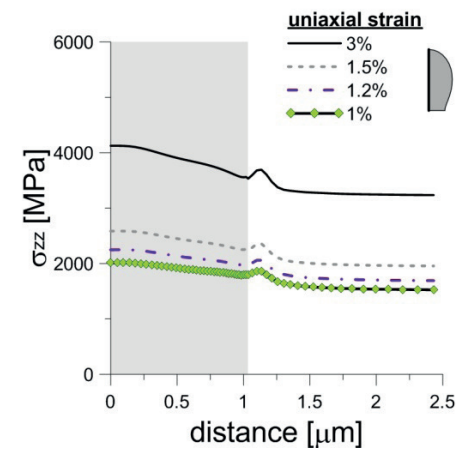

Fig. 4f. (Inclusion of elongated cross-section (Fig. 1d) with the longest axis oriented parallel to the loading direction.) Opening stress (σ_{zz}) distribution along the vertical line. u_y/u_z=-0.5

TABLE 1

Maximum opening and effective stresses ($\sigma_e = \sqrt{3J_2} = \sqrt{\frac{3s_{ij}s_{ij}}{2}}$, where J_2 is the second invariant of the deviatoric stress) in and around a cylindrical inclusion with u_y/u_z=-0.5

Loading strain	Max. opening Stress inside (effective stress) Horizontal line MPa	Max. opening Stress outside Horizontal line MPa	Max. opening Stress inside (effective stress) Vertical line MPa	Max. opening Stress outside Vertical line MPa
1%	1690 (1340)	1510	1680	1730
1.2%	1870 (1400)	1680	1860	1920
1.5%	2180 (1480)	1950	2140	2210
3%	3640 (1900)	3230	3450	3540

TABLE 2

Maximum opening and effective stresses in and around an inclusion of elliptical cross-section with the major axis oriented perpendicular to the loading direction (Fig. 1a). u_y/u_z=-0.5

Loading strain	Max. opening Stress inside inclusion (effective stress) Horizontal line MPa	Max. opening Stress outside inclusion Horizontal line MPa	Max. opening Stress inside inclusion (effective stress) Vertical line MPa	Max. opening Stress outside inclusion Vertical line MPa
1%	1560 (1430)	1510	1540	1600
1.2%	1740 (1510)	1680	1710	1780
1.5%	2020 (1600)	1940	1970	2070
3%	3340 (1960)	3222	3230	3390

Maximum opening end effective stresses in and around an inclusion of elongated shape with the longest axis oriented in the loading direction (Fig. 1d). u_y/u_z=-0.5

Loading strain	Max. opening Stress inside inclusion (effective stress) Horizontal line MPa	Max. opening Stress outside inclusion Horizontal line MPa	Max. opening Stress inside inclusion (effective stress) Vertical line MPa	Max. opening Stress outside inclusion Vertical line MPa
1%	2560 (2030)	1510	2010	1870
1.2%	2900 (2220)	1680	2250	2060
1.5%	3340 (2420)	1940	2580	2360
3%	5260 (3210)	3230	4130	3690

Fig. 5 shows representative results of the stress distribution in and around an inclusion of cylindrical shape under a relatively low constraint: u_y/u_z=-0.7. Fig. 6 shows the results for the stronger constraint of u_y/u_z=-0.3.

Qualitatively similar stress distributions were obtained for other inclusion shapes. The maximum stress values for these two constraint levels are listed in Tables 4 and 5, respectively.
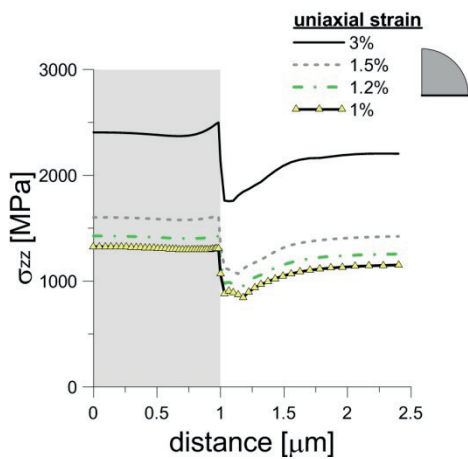

Fig. 5a. (Cylindrical inclusion.) Opening stress distribution along the horizontal line. u_y/u_z=-0.7
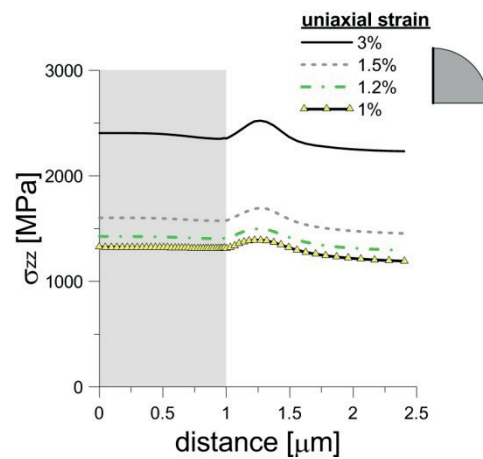

Fig. 5b. (Cylindrical inclusion.) Opening stress distribution along the vertical line. u_y/u_z=-0.7
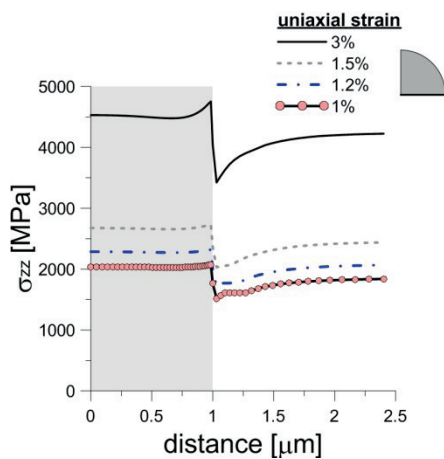

Fig. 6a. (Cylindrical inclusion.) Opening stress (σ_{zz}) distribution along the horizontal line. u_y/u_z=-0.3
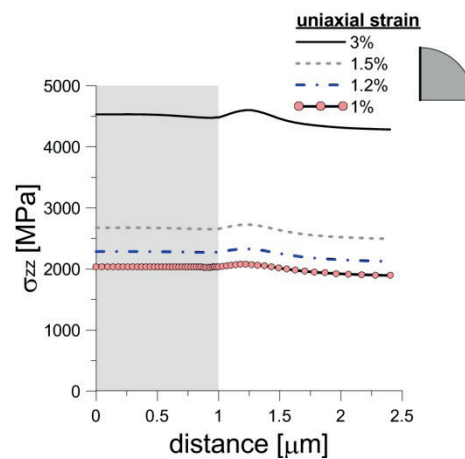

Fig. 6b. (Cylindrical inclusion.) Opening stress (σ_{zz}) distribution along the vertical line. u_y/u_z=-0.3

TABLE 4

Maximum opening end effective stresses in and around a spherical inclusion with $u_y/u_z=-0.7$

Loading strain	Max. opening Stress (σ_{zz}) inside (effective stress) Horizontal line MPa	Max. opening Stress (σ_{zz}) outside Horizontal line MPa	Max. opening Stress (σ_{zz}) inside (effective stress) Vertical line MPa	Max. opening Stress (σ_{zz}) outside Vertical line MPa
1%	1330 (1350)	1160	1330	1390
1.2%	1420 (1360)	1270	1430	1500
1.5%	1620 (1420)	1430	1600	1700
3%	2500 (1640)	2220	2410	2520

TABLE 5

Maximum opening end effective stresses in and around a spherical inclusion with

$u_y/u_z=-0.3$

Loading strain	Max. opening Stress (σ_{zz}) inside (effective stress) Horizontal line MPa	Max. opening Stress (σ_{zz}) outside Horizontal line MPa	Max. opening Stress (σ_{zz}) inside (effective stress) Vertical line MPa	Max. opening Stress (σ_{zz}) outside Vertical line MPa
1%	2007 (1350)	1850	2040	2080
1.2%	2320 (1440)	2090	2290	2330
1.5%	2730 (1570)	2460	2690	2730
3%	4750 (2220)	4250	4530	4600

4. Discussion and conclusions

The results presented in this paper provide calculated stress distributions within elementary cells containing inclusions of various shapes and orientations. An elementary cell was positioned in the domain in front of the crack along the axis of the specimen. The in-plane constraint level was controlled by the ratio u_y/u_z. This scenario is idealized because it does not take into account the possible subcritical growth of the crack. Using the hypothesis presented in [4], subcritical crack growth, manifested by nucleation, growth and coalescence of voids starts when the quantity A, computed from the equation $A = \varepsilon_{pl} \exp\left(\dfrac{\sigma_m}{\sigma_0}\right)$ reaches a value of 3 for Hardox-400 steel. Here, ε_{pl} is the accumulated effective plastic strain, σ_m is the average hydrostatic stress and σ_0 is the yield strength. Thus, the lowest curve in Fig. 3, recorded at 33% of the critical deflection, represents the state before the onset of subcritical crack growth. The A value is 0.98. However, the plastic strain within the elementary cell is 0.022, and at this strain level many inclusions have already fractured if we assume that the critical stress is 1600 MPa. The curve in the middle represents the strain in front of the already growing crack. Thus, the voids closest to the crack front must have already joined together and have been absorbed by the moving crack front.

According to the stress values listed in Tables 1-5, void nucleation starts with the failure of long narrow voids with major axes oriented parallel to the loading direction. When elongated inclusions are oriented perpendicularly to the loading direction, they are more likely to debond than crack. These tables also indicate the degree of influence of the in-plane constraint on void nucleation. However, it should be noted that a nucleated void may grow either as a void or as a micro-crack. The greater the constraint, the greater the probability of cleavage fracture.

REFERENCES

[1] A.Neimitz, U. Janus, Analysis of stress and strain fields in and around inclusions of varius shapes in a cylindrical specimen loaded in tension. Archives of Metallurgy and Materials **61**, 2A, 569-576 (2016).

[2] I. Dzioba, R. Pała, T. Pała, Temperature dependency of fracture toughness of high-strength ferritic steel Hardox-400, Acta Mechanica et Automatica **7**, 4, 222-225, (2013), DOI 10.2478/ama-2013-0037.

[3] J. Gałkiewicz, Microscopically based calibration of the

1592

cohesive model, Journal of Theoretical and Applied Mechanics 53, 2, 477-485,(2015), DOI: 10.15632/jtam-pl.**53**.2.477.

[4] A. Neimitz, Ductile fracture mechanisms in the high-strength steel Hardox-400.Microscopic observations and numerical stress-strain analysis. Procedia Material Science, 3, Elsevier, Science Direct, 270 – 275 (2014).